Surfaces and Interfaces 88 (2026) 109055

Contents lists available at ScienceDirect

Surfaces and Interfaces

journal homepage: www.sciencedirect.com/journal/surfaces-and-interfaces

Utilizing *ab initio* atomistic thermodynamics to unravel the impact of oxygen partial pressure and atmospheric annealing on a thin NiOx film for efficient inverted perovskite solar cells

Waranchit Ruengsrisang [a], Pakpoom Reunchan [b], Watchara Liewrian [a], Non Thongprong [c,*]

[a] *Department of Physics, Faculty of Science, King Mongkut's University of Technology Thonburi, 126 Pracha-Uthid Road, Bang Mot, Thung-Khru, Bangkok 10140, Thailand*

[b] *Department of Physics, Faculty of Science, Kasetsart University, Chatuchak, Bangkok 10900, Thailand*

[c] *Nanoscience and Nanotechnology Graduate Program, Faculty of Science, King Mongkut's University of Technology Thonburi, 126 Pracha-Uthid Road, Bang Mot, Thung-Khru, Bangkok 10140, Thailand*

ARTICLE INFO

Keywords:
Ab Initio atomistic thermodynamics
Density functional theory
Nickel oxide
Perovskite solar cells
Surface free energy
Thin film annealing

ABSTRACT

Thermal annealing is a critical post-processing step for improving NiO_x thin films, which serve as hole transport layers in high-efficiency inverted perovskite solar cells. Recent experimental studies highlight the importance of annealing atmosphere, particularly oxygen and nitrogen partial pressures, but an atomistic understanding remains limited. Here, we use density functional theory (DFT+U) with *ab initio* atomistic thermodynamics to examine NiO_x(001) surfaces under O_2/N_2 environments. A key contribution of this work is the development of a selective-fixation asymmetric slab energy (SFAE) method, which enables robust surface-free-energy evaluation for asymmetric slab models and the construction of thermodynamically consistent surface phase diagrams over broad temperature and chemical-potential conditions. Our results show that O_2-rich environments enhance the p-type character of NiO_x by stabilizing nickel vacancies and healing oxygen vacancies through chemisorption. In contrast, N_2 annealing does not produce reactive atomic nitrogen and therefore cannot generate substitutional N defects. Residual physisorbed O_2 and N_2 species are weakly bound and desorb readily, enabling clean surface preparation after defect healing. This study provides atomic-level insight into NiO_x stability under realistic annealing conditions and offers practical guidance for tuning surface properties through controlled oxygen stoichiometry, while also establishing a theoretical basis for future catalytic studies.

1. Introduction

Perovskite solar cells (PSCs) have rapidly achieved high power conversion efficiencies (PCEs), with the conventional n-i-p architecture featuring TiO_2 as the electron transport layer (ETL) and spiro-OMeTAD as the hole transport layer (HTL) being the most widely adopted design [1–3]. However, this structure typically relies on high-temperature processing of mesoporous TiO_2, which hinders scalable and low-cost fabrication. In contrast, the p-i-n configuration offers a simpler, low-temperature process, but often at the cost of reduced efficiency. To improve the stability and performance of p-i-n PSCs, inorganic HTLs have been explored as alternatives to organic materials such as PEDOT:PSS, which suffer from degradation due to acidity [4]. Among these, nickel oxide (NiO_x) stands out due to its high transparency, wide bandgap, outstanding hole selectivity, low cost, and excellent chemical and thermal stability [4,5].

The surface chemistry of NiO_x is highly complex due to the coexistence of multiple nickel oxidation states, including Ni^{2+}, Ni^{3+}, and higher-valent Ni species [6]. While stoichiometric NiO containing only Ni^{2+} is intrinsically insulating, the electrical conductivity of non-stoichiometric NiO_x is strongly influenced by nickel and oxygen vacancies (V_{Ni} and V_O) as well as their interstitial counterparts [7]. In particular, V_{Ni} defects enhance p-type conductivity by generating Ni^{3+}-associated hole states [7]. However, excessive concentrations of V_{Ni} and Ni^{3+} can trigger surface redox reactions, ultimately compromising the stability of perovskite solar cells (PSCs) [6,8].

* Corresponding author.
E-mail address: non.tho@kmutt.ac.th (N. Thongprong).

https://doi.org/10.1016/j.surfin.2026.109055
Received 22 September 2025; Received in revised form 27 February 2026; Accepted 18 March 2026
Available online 19 March 2026

Given these sensitivities, controlling the optimal concentration of surface defects through tuning the oxygen partial pressure during NiO_x film deposition and post-annealing remains a critical—yet unresolved—challenge [9–11]. Notably, the literature reports conflicting trends. For example, Zhao et al. identified 30% O_2 at 400 °C as the optimal $O_2/(O_2+N_2)$ ratio and annealing temperature for maximizing PCE [12]. In contrast, Seok et al. reported that NiO_x films sputtered in pure Ar yield superior device performance [10], while Haider et al. found that oxygen-deficient conditions enhance conductivity and performance [9]. These discrepancies highlight the need for a deeper atomistic understanding of how oxygen and nitrogen environments regulate NiO_x surface defects and, consequently, device behavior.

In this work, we integrate DFT with *ab initio* atomistic thermodynamics to investigate the interaction between O_2 and N_2 gases with NiO_x surfaces during thermal annealing and how these interactions impact the electronic properties of NiO_x. We systematically explore the stability of nickel vacancies, oxygen vacancy healing, and nitrogen adsorption on NiO_x surfaces. While the Reuter and Scheffler formalism [13,14] is the conventional framework for constructing surface phase diagrams as functions of temperature and chemical potentials, it is not directly applicable to asymmetric slab models without additional corrections [15]. To address this limitation, we developed a new approach—the Selective Fixation Asymmetric Slab Energy (SFAE) method—which reformulates the surface free energy calculation to enable accurate and efficient treatment of asymmetric surfaces. Our results show that O_2 adsorption promotes Ni-vacancy formation and effectively heals oxygen vacancies, thereby enhancing the intrinsic p-type character of NiO_x. Although substitutional nitrogen would introduce acceptor states near the valence band maximum, our analysis demonstrates that thermal annealing in N_2 cannot supply the reactive atomic nitrogen required for such incorporation. These insights provide a fundamental basis for tuning NiO_x surface properties through controlled oxygen stoichiometry, with direct implications for optimizing NiO_x-based hole-transport layers in perovskite solar cells and for guiding future catalytic studies.

2. Computational methodology

In this work, we restrict our analysis to neutral defects. Although NiO_x is a p-type oxide, the formation energies of defects such as V_{Ni} can depend on the Fermi level and vary across different charge states. Calculating charged defects in slab geometries presents significant challenges. These include the need for compensating background charges, artificial electrostatic interactions across the vacuum region, and the difficulty of assigning a well-defined charge state to a surface-localized defect. Without specialized correction schemes, these issues can introduce substantial uncertainty into the energetics of charged defects. By focusing on neutral defects, we obtain a consistent and robust baseline for evaluating thermodynamic trends in nickel and oxygen vacancies under the gas chemical potentials relevant to this study. This approach provides a foundational framework, and a comprehensive treatment of charged defects—together with experimental validation—will be pursued in future work.

2.1. Computational details for bulk NiO

To establish a reliable computational setup, we conducted convergence tests with particular focus on selecting the Hubbard U parameter by benchmarking against experimental values for the lattice constant, band gap [16], and magnetic moment per Ni site [17,18]. All calculations were performed using the Quantum ESPRESSO package [19]. As detailed in Supporting Information (Section 1), our tests indicate that the revised Perdew-Burke-Ernzerhof functional for solids (PBEsol) [20,21] combined with the projector augmented wave (PAW) method and a Hubbard U of 6 eV with spin polarization enabled provides the best agreement with experiments while maintaining computational efficiency.

For total energy self-consistent field (SCF) and density of states non-self-consistent field (NSCF) calculations, we used the tetrahedron method with Blöchl corrections [22]. Structural relaxations were performed with Gaussian smearing (0.01 Ry) and Davidson iterative diagonalization. Convergence thresholds were set at 7.35×10^{-4} Ry/Bohr (0.02 eV/Å) for atomic forces and 1.50×10^{-5} Ry for ionic energy minimization. The SCF energy convergence was set to 1.00×10^{-6} Ry for structural relaxation and tightened to 1.00×10^{-8} Ry for the initial SCF steps preceding NSCF calculations. Brillouin zone integrations employed Monkhorst-Pack (MP) k-point grids [23] of $(3 \times 3 \times 1)$, $(4 \times 4 \times 1)$, and $(8 \times 8 \times 1)$ for relaxation, SCF, and NSCF steps, respectively, corresponding to k-point spacing of ~0.3 and ~0.2 $Å^{-1}$. Plane-wave cutoffs were set at 80 Ry for wavefunctions and 800 Ry for charge density and potential.

2.2. Computational details for surface slabs

We employed an asymmetric NiO(001) slab model with a large vacuum region to minimize dipole effects in surface energy calculations. Convergence tests for slab thickness and vacuum spacing were performed (see Supporting Information, Section 2). The results indicate that a model with five atomic layers and a 20 Å vacuum, as illustrated in Fig. 1 (left), reproduces key properties of thicker slabs (nine layers, 20–30 Å vacuum). Using a 15 Å vacuum yields a surface free energy error of less than 6×10^{-5} eV/$Å^2$ and less than 2×10^{-5} eV/$Å^2$ compared to the nine-layer slab. From k-point convergence tests, we adopted MP grids of $3 \times 3 \times 1$ (0.4 $Å^{-1}$) for relaxation, $4 \times 4 \times 1$ (0.3 $Å^{-1}$) for SCF, and $8 \times 8 \times 1$ (0.15 $Å^{-1}$) for NSCF calculations.

To mimic NiO thin films, the bottom three atomic layers were fixed to simulate the bulk, while the top two were fully relaxed. The NiO(001) surface was selected due to its prevalence as the dominant facet [24–27]. We evaluated three representative adsorption sites (Fig. 1, right): Ni sites (i), bridging Ni/hollow sites (ii), and O sites (iii). Dispersion interactions were included via the DFT-D3 van der Waals correction [28], ensuring accurate treatment of physisorption, especially for inert molecules like N_2. The correction was also applied to O_2 adsorption for consistency.

3. Theory

In this section, we described the use of *ab initio* atomistic thermodynamics to determine the influence of ambient gas on nickel oxide film annealing by evaluating the surface free energy (γ^{surf}) of different surface phases. This section was divided into two subsections: Section 3.1, deriving the standard method's equations of the NiO surface system, and Section 3.2, introducing our SFAE method.

3.1. Ab initio thermodynamics for NiO surface in O_2 and N_2 environments

We modeled the thermal annealing of NiO films as surface equilibria with O_2 and N_2 gas reservoirs, allowing atomic exchange at fixed temperature (T) and pressure (P). To determine the stability of a surface, we follow the scheme proposed by Reuter and Scheffler [13,14], which is referred to as the standard method. The surface free energy at temperature T and partial pressures P_{O_2} and P_{N_2}, denoted as $\gamma^{surf}(T, P_{O_2}, P_{N_2})$, is given by

$$\gamma^{surf}(T, P_{O_2}, P_{N_2}) = \frac{1}{2A}\left[G^{slab}_{NiO} - N_{Ni}\mu_{Ni}(T) - N_O\mu_O(T,\ P_{O_2}) - N_N\mu_N(T,\ P_{N_2})\right], \quad (1)$$

where G^{slab}_{NiO} is the Gibbs free energy of the slab, including the two-equivalent surface with the area A, and N_{Ni}, N_O, N_N, μ_{Ni}, μ_O, and μ_N are the number and the chemical potential of Ni, O, and N atoms/species in the system, respectively. The concepts of constrained thermodynamic

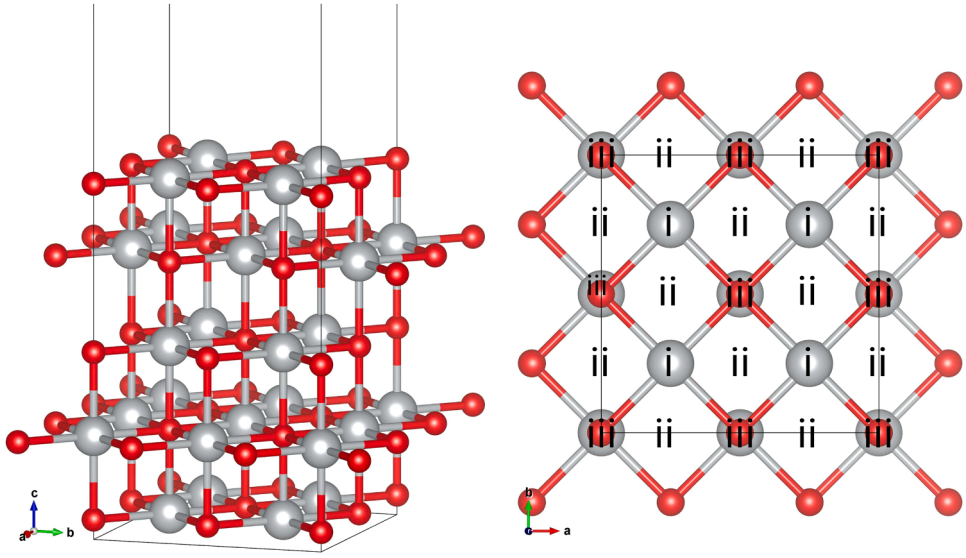

Fig. 1. Slab model of NiO(001) used in this study (left). Three representative adsorption sites are considered: (i) the Ni site, (ii) the bridging Ni/hollow site, and (iii) the O site (right).

equilibrium were employed in this derivative to integrate the thermodynamic formalism with density functional theory at the atomic level. In Eq. (1), the chemical potentials of Ni and O are related through Gibbs free energy per formula unit of bulk NiO (g_{NiO}^{bulk}),

$$\mu_{Ni} + \mu_O = g_{NiO}^{bulk}. \tag{2}$$

Additionally, the surrounding O_2 and N_2 gas reservoirs are also constrained by an equilibrium. The chemical potential of O and N can be considered in terms of the difference (Δμ) between Gibbs free energy and the DFT total energy at 0 K, under the thermodynamic equilibrium constraint, as follows:

$$\Delta\mu_O(T,\ P_{O_2}) = \mu_O(T,\ P_{O_2}) - E_O^{tot}, \tag{3}$$

and

$$\Delta\mu_N(T,\ P_{N_2}) = \mu_N(T,\ P_{N_2}) - E_N^{tot}, \tag{4}$$

where the atomic total energies of E_O^{tot} and E_N^{tot} are calculated from O_2 and N_2 molecules by $E_O^{tot} = E_{O_2}^{tot}/2$ and $E_N^{tot} = E_{N_2}^{tot}/2$, respectively. Inserting Eqs. (2)–(4) into Eq. (1) expresses in DFT total energies combined with chemical potential and Gibbs free energies:

$$\gamma^{surf}(T,P_{O_2},P_{N_2}) = \frac{1}{2A}[G_{NiO}^{slab} - N_{Ni}g_{NiO}^{bulk} - (N_O - N_{Ni})E_O^{tot} - N_N E_N^{tot} - (N_O - N_{Ni})\Delta\mu_o(T,\ P_{O_2}) - N_N\Delta\mu_N(T,\ P_{N_2})] \tag{5}$$

The difference between the Gibbs free energies of the slab and the Gibbs free energies per formula unit of bulk can be replaced by corresponding total energies, with the reason that the vibrational energy and entropy contributions to this difference of Gibbs free energies are negligible and cancel each other out [14,29]. Resulting in the surface free energy at a specific temperature and partial pressure, expressed as a linear function of the environmental gases in $\Delta\mu_O$and $\Delta\mu_N$ space,

$$\gamma^{surf}(T,P_{O_2},P_{N_2}) = \frac{1}{2A}[E_{NiO}^{slab} - N_{Ni}E_{NiO}^{tot} - (N_O - N_{Ni})E_O^{tot} - N_N E_N^{tot} - (N_O - N_{Ni})\Delta\mu_o(T,\ P_{O_2}) - N_N\Delta\mu_N(T,\ P_{N_2})] \tag{6}$$

The variation of the chemical potentials in Eq. (6) was determined by the condition of thermodynamic equilibrium. Their dependence on temperature (T) and pressure (P), relative to a reference state ($\Delta\mu_N^r$) at standard pressure (P^o), is given by:

$$\Delta\mu_O(T,P_{O_2}) = \Delta\mu_O^r(T,P^o) + \frac{1}{2}k_B T ln\left(\frac{P_{O_2}}{P^o}\right), \tag{7}$$

and

$$\Delta\mu_N(T,P_{N_2}) = \Delta\mu_N^r(T,P^o) + \frac{1}{2}k_B T ln\left(\frac{P_{N_2}}{P^o}\right), \tag{8}$$

where P^o = 1atm, k_B is the Boltzmann constant, and $\Delta\mu_O^r(T,P^o)$ and $\Delta\mu_N^r(T,P^o)$ are the chemical potentials at the reference states. In our work, the enthalpy changes and entropy used to calculate the chemical potentials at the reference state are taken from the CRC Handbook of Chemistry and Physics thermochemical tables [30]. Our calculated chemical potentials at the reference state (atmospheric pressure P^o) are shown in Table 1. Calculation details were discussed in the Supporting Information, Section 3.

3.2. Selective fixation asymmetric slab energy (SFAE) method

We propose the SFAE method to calculate the surface free energy of an asymmetric slab model, which contains a bulk-like bottom region and a surface-active top region. This method builds upon the standard approach for symmetric slabs and incorporates the central conceptual idea introduced by the simultaneous equation method of Stuart and Sohlberg [15]. Their study demonstrated that the two terminations of an asymmetric slab can be separated into individual surface energy contributions through a least squares construction. This methodology enables us to extract surface free energy specifically from the surface-active top region, as illustrated in the light grey region in

Table 1
Reference chemical potential differences, $\Delta\mu_O^r(T,P^o)$ and $\Delta\mu_N^r(T,P^o)$ over the temperature range considered in this study.

T	$\Delta\mu_O^r(T,P^o)$	$\Delta\mu_N^r(T,P^o)$
300 K	−0.27	−0.25
400 K	−0.38	−0.35
500 K	−0.49	−0.46
600 K	−0.61	−0.57
700 K	−0.73	−0.68
800 K	−0.85	−0.79
900 K	−0.97	−0.91
1000 K	−1.10	−1.03

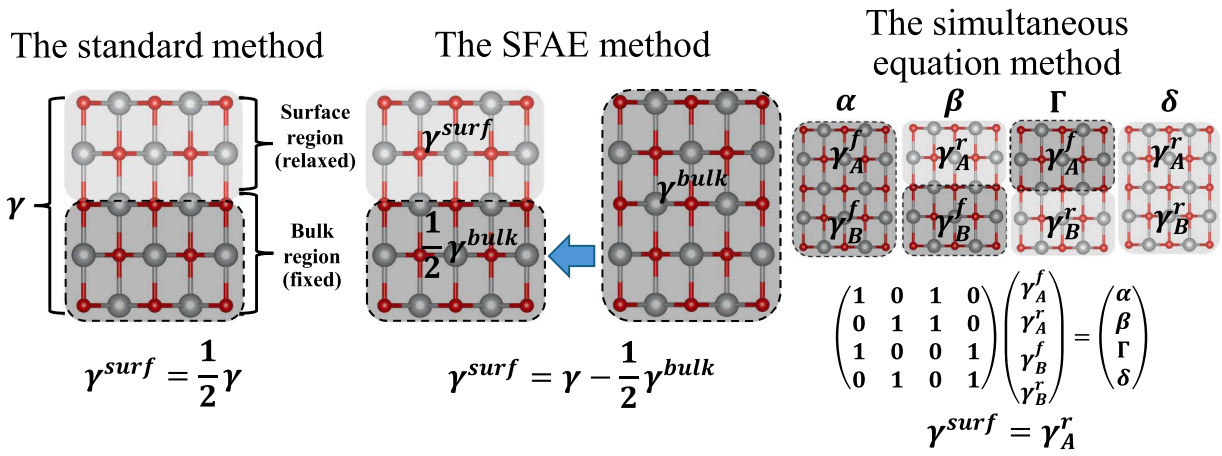

Fig. 2. Schematic illustration of the three surface free energy calculation methods. The slab model is divided into a bulk-like region (dark gray, fixed NiO layers) and a surface-active region (light gray, relaxed NiO layers).

Fig. 2 **(left)**. This insight is valuable because it establishes that the energy of the surface-active termination can in principle be isolated from the total slab energy. The SFAE method uses this insight in a simpler and more efficient way by determining the energy contribution of the bulk-like bottom region once and then removing it from the total surface energy. The remaining energy therefore corresponds entirely to the surface free energy of the top surface-active region. This provides a direct and computationally economical alternative to solving the full set of simultaneous equations—while retaining the same conceptual rigor.

In terms of computational cost, the difference is substantial. As illustrated in Fig. 2 **(right),** To generate the surface energy contributions of the top region A and the bottom region B using the simultaneous equation method, four total energy calculations are required for each surface model. These include the total energies of the slab before geometric optimization, after full geometric optimization, with only region A relaxed while region B is frozen, and with only region B relaxed while region A is frozen. The lattice parameters remain fixed in all four calculations. As a result, the cost of evaluating the surface energy of a single asymmetric slab is multiplied by a factor of four.

In contrast, the SFAE method requires only a single converged slab calculation for each surface phase once the bulk-like reference is established, which significantly reduces computational effort and improves numerical stability. Finally, we note that the SFAE method would not be possible without the conceptual foundation provided by the simultaneous equation method. The ability to simplify the calculation relies entirely on the valuable evidence presented by Stuart and Sohlberg that the energies of the two slab terminations can indeed be treated as fully separable quantities.

The methodology of the SFAE method is straightforward: to determine the surface free energy of the top surface region, we subtract the bulk-like surface energy contribution from the total surface free energy of the slab. This yields the surface free energy (γ) corresponding to each surface phase model, as described by the following equation:

$$\gamma^{surf} = \gamma - \frac{1}{2}\gamma^{bulk}, \tag{9}$$

where γ is the cumulative surface free energy containing contributions from both the top and bottom surfaces and γ^{bulk} only representing the bulk-like symmetric slab, obtained from an unrelaxed pristine slab. Both γ and γ^{bulk} are calculated using Eq. (6) without the $\frac{1}{2}$ factor. The value of γ^{bulk} is treated as a constant and used to subtract the bulk energy contribution from each surface phase model.

Table 2 presents the bulk energy contributions and the corresponding surface free energies of the asymmetric slab calculated using three different approaches: the standard method, Stuart and Sohlberg's simultaneous equations method, and the SFAE method, yielding values of 61.72, 62.04, and 62.04 meVÅ^{-2}, respectively. Our SFAE results show good agreement with the simultaneous equations method at the PBEsol+U level and are consistent with previous theoretical studies [31, 32] when the differences in methodology are considered. Both Reference 31 and Reference 32 used the PBE+U functional, which is different from the PBEsol+U functional employed in the present work. This difference in exchange and correlation treatment, together with the well-known sensitivity of NiO surface energetics to the chosen value of the Hubbard U parameter, explains the numerical range of their reported surface energies, namely 54.2 and 59.0 meV/Å^2. Reference 31 also used a 2 × 1 surface model instead of the 1 × 1 model used in Reference 32 and in our work, although this difference does not influence the final surface energy because the value is normalized by surface area. The main variations arise from the different U values selected according to each author's assumptions. In contrast, the LDA+U results reported in References 33 and 34 are not reliable because the LDA functional significantly overbinds and underestimates lattice constants, which leads to inaccurate surface and defect energetics. We provide our Python code for calculating the asymmetric surface free energy using the simultaneous equations method with implementation details in the Supporting Information, Section 4.

Table 2
The asymmetric surface free energy of the perfect NiO(001) surface from different methods at the PBEsol+U level.

Methods	Surface free energy (meVÅ^{-2})	Bulk surface free energy (meVÅ^{-2})
Standard	61.72	61.72
SFAE	61.39	62.04
Simultaneous equation	61.40	62.04
References	54.20[a], 59.00[b], 80.40[c], 83.01[d]	-

[a] PBE+U [31] c LDA+U [33].
[b] PBE+U [32] d LDA+U [34].

The calculation of charged defects on the surface presents significant methodological challenges and is not the focus of this work. The point defect formation energy, ΔE_f, in our work is calculated based on the general formalism at the neutral charge defect on the NiO_x(001) surface. Which can be simplified as

$$\Delta E_f = E^{tot}_{surf,D} - E^{tot}_{surf,P} - \sum_i N_i \mu_i \tag{10}$$

where $E^{tot}_{surf,D}$ and $E^{tot}_{surf,P}$ are the total energies of the surface with and without point defects, respectively. The integer N_i indicates the number of atom types i that have been removed ($N_i < 0$) from or added ($N_i > 0$)

to the surface to create the defect and μ_i is the chemical potential of atomic species *i*. Note that we align the negative and positive values of the chemical potential with the processes of adding or removing atoms. The higher the energy value, the less likely the defect will form spontaneously. We also use the concept of adsorption energy, ΔE_{ad}, to measure how strongly an atom or molecule binds to a surface by following the equation,

$$\Delta E_{ad} = E^{tot}_{surf+at/mo} - \left(E^{tot}_{surf} + E^{tot}_{at/mo}\right), \quad (11)$$

where $E^{tot}_{surf+at/mo}$ is the total energy of the surface and the adsorbate atom or molecule, E^{tot}_{surf} is the total energy of the surface without the adsorbate, and $E_{at/mo}$ is the total energy of the atom or molecule in isolation. A negative energy value indicates that the adsorption process is exothermic, which means that the adsorption is energetically favorable. A positive energy value indicates an endothermic adsorption process; energy is usually needed to bind the adsorbate to the surface, which is unfavorable.

We investigated the nature of defects during NiO film preparation, focusing on two primary point defects. The first is the Ni vacancy, which is the dominant defect in NiO and responsible for its intrinsic p-type semiconducting behavior. The second is the O vacancy, which may form during synthesis. Interstitial defects are excluded from this study due to their high formation energies [35]. To explore surface oxidation and reduction processes, we considered the possible surface phases that can arise within the full range from the O-poor limit to the O-rich limit under varying oxygen gas pressures.

We calculated the formation energies of point defects for O-vacancy (V_O) and Ni-vacancy (V_{Ni}) on the NiO(001) surface (Table 3, Section 4), which are 4.88 and 3.57 eV, respectively. In comparison, their formation energies in bulk NiO are 4.40 and 1.18 eV, respectively [36]. These results indicate that Ni-vacancies are energetically more readily formed than O-vacancies in both bulk and surface NiO. However, V_{Ni} formation is more difficult on the surface due to the increased formation energy, consistent with experimental findings that NiO is typically metal-deficient [36].

4. Results & discussion

To reduce the complexity of analyzing the effects of O_2 and N_2 partial pressures on the nickel oxide surface, we divide our investigation into three parts. In Section 4.1, we first examine the surface phase diagram of nickel oxide in an O_2 environment at 600 and 800 K, which are within the typical annealing temperature range, followed by 300 and 400 K (see the Supporting Information, Section 5) to represent the cooling and room temperature conditions. Section 4.2 then explores the influence of N_2 gas, using the O_2 background condition as a reference while varying the N_2 partial pressure. In Section 4.3, we investigate the combined effect of both O_2 and N_2 partial pressures on the surface phase behavior. Finally, Section 4.4 contextualizes our findings within the existing literature and highlights key outlooks for future investigation.

Table 3
Summary of point defect formation energies (ΔE_f) and adsorption energies (ΔE_{ad}) for O and O_2 species on NiO/NiO_x(001) surfaces.

Category	Phase Description	Energy Type	Energy (eV)
Defect Formation	(P1) V_O on NiO(001) surface	ΔE_f	4.88
	(P2) V_{Ni} on NiO(001) surface	ΔE_f	3.57
	(P3) V_{Ni} with adsorbed O_2 at a neighboring Ni site	ΔE_f	3.21
	(P4) Bridging V_O ($V_{O,br}$)	ΔE_f	–1.20
O Adsorption	(P5) V_O-healed surface (O filling a V_O) (O_{V_O})	ΔE_{ad}	–4.88
O_2 Adsorption	(P6) O_{V_O} with a bridging O at Ni sites (O_{V_O}+O_{br})	ΔE_{ad}	–3.67
	(P7) O_2 adsorbed on Ni site of perfect surface (O_2@Ni)	ΔE_{ad}	–1.03
	(P8) O_2 adsorbed on Ni site adjacent to V_{Ni} (O_2@Ni-V_{Ni})	ΔE_{ad}	–1.40

4.1. Surface phase diagram in O_2 environment

We constructed three foundational surface models: perfect, O-vacancy (V_O), and Ni-vacancy (V_{Ni}) NiO(001) surfaces. Using the periodic adsorption sites labeled in Fig. 1 (right), we evaluated all plausible adsorption positions for oxygen species on the NiO/NiO_x(001) surfaces. From here, we identified eight representative surface phases, summarized in Table 3, along with their formation and adsorption energies.

The surface phase diagram of NiO/NiO_x(001) in an O_2 atmosphere was constructed using our SFAE method by expressing the surface free energy of each configuration as a linear function of $\Delta\mu_O(T, P_{O_2})$, constrained within the O-poor and O-rich limits ($-3.30 < \Delta\mu_O(T, P_{O_2}) < 0$; see Supporting Information, Section 6). Plotting these free energies at a given temperature and pressure allows identification of the lowest-energy surface and the corresponding phase boundaries.

Some phase boundaries appear at oxygen partial pressures far outside experimentally accessible conditions. These transitions are included only for thermodynamic completeness. For practical interpretation, the experimentally relevant phases are those within typical laboratory oxygen pressures, approximately 10^{-6} to 1 atm.

The surface phase diagrams of the base cases—perfect, V_O-, and V_{Ni}-NiO(001) surfaces—were drawn in Figs. 3–5. Fig. 3**a**–**c** show the phase transitions originating from the perfect NiO(001) surface under increasing O_2 partial pressure. Two notable transitions occur near the O-rich limit. The first transition appears at $\Delta\mu_O \approx -0.52$ eV, corresponding to O_2 partial pressures of approximately 2.40×10^{-7}, 6.42×10^{-3}, 2.53×10^{2}, and 6.69×10^{4} atm at 300, 400, 600, and 800 K, respectively. At

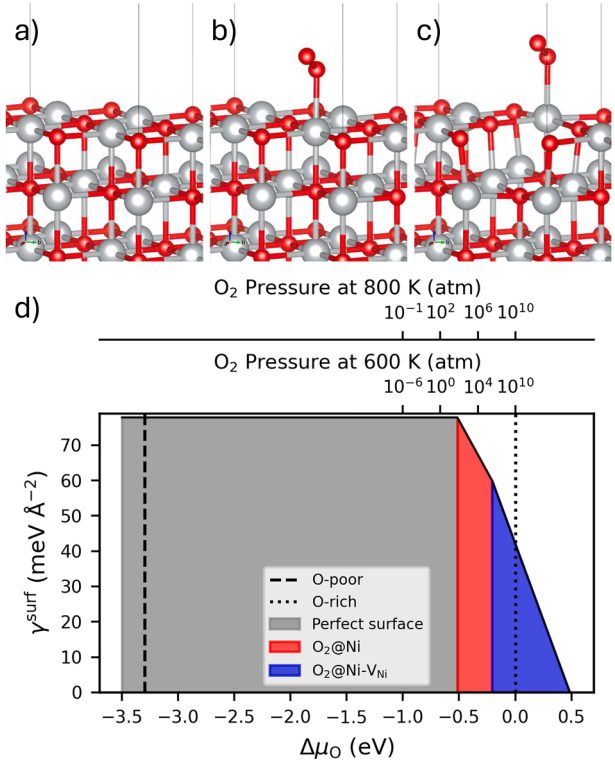

Fig. 3. Relaxed atomic structures of (a) perfect surface, (b) O_2 adsorbed on a Ni site (P7), and (c) O_2 adsorbed on the Ni site adjacent to V_{Ni} (P8). Gray and red atoms represent Ni and O, respectively. (d) Surface free energy as a function of $\Delta\mu_O$. Dashed and dotted lines indicate the O-poor and O-rich limits, respectively. The top axes show corresponding O_2 pressures at 600 and 800 K.

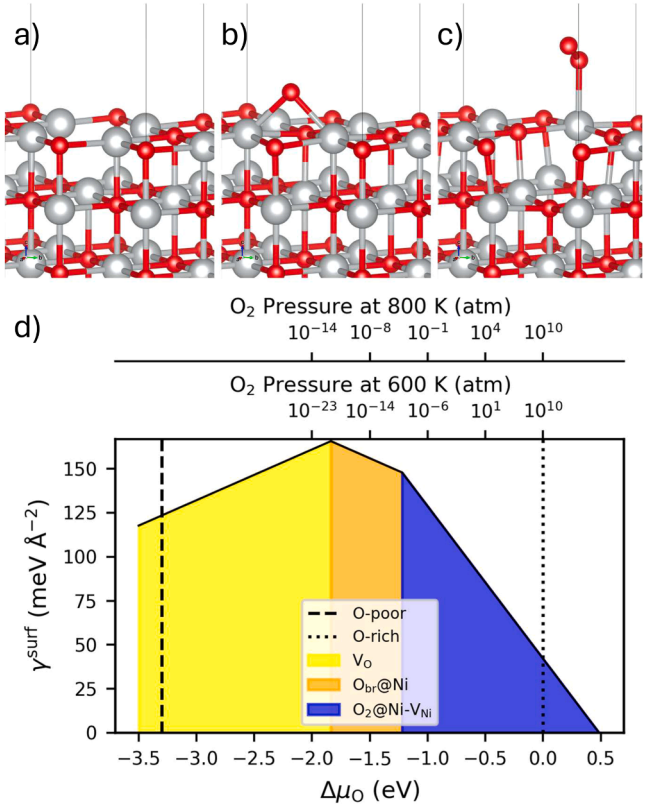

Fig. 4. Relaxed atomic structures of representative surface phases: (a) V_O surface (P1), (b) V_O-healed surface with a bridging O atom adsorbed on a Ni site (P6), and (c) O_2 adsorbed on the Ni site adjacent to V_{Ni} (P8). Gray and red atoms represent Ni and O, respectively. (d) Surface free energy as a function of $\Delta\mu_O$. Dashed and dotted lines, respectively, indicate the O-poor and O-rich limits. The top axes show corresponding O_2 pressures at 600 and 800 K.

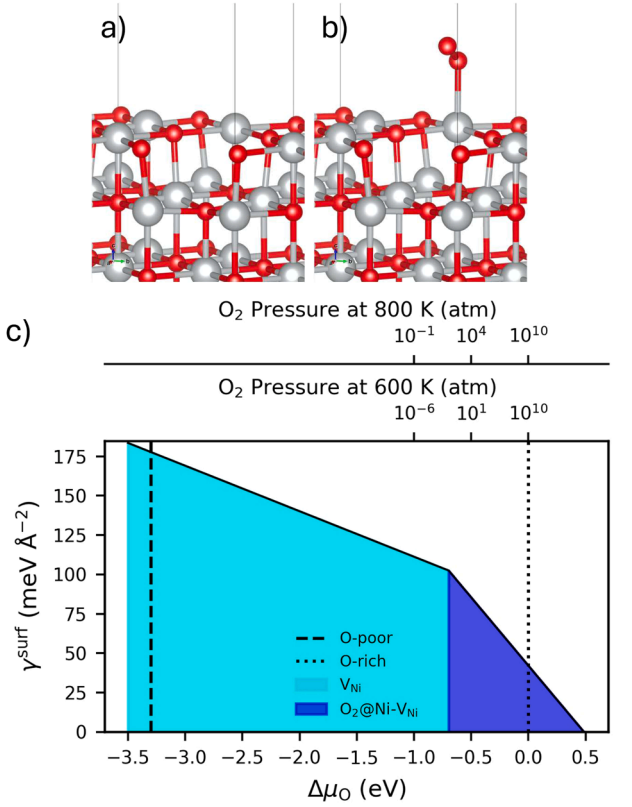

Fig. 5. Relaxed atomic structures of representative surface phases: (a) V_{Ni} surface (P2), and (b) O_2 adsorbed on the Ni site adjacent to V_{Ni} (P8). Gray and red atoms represent Ni and O, respectively. (c) Surface free energy as a function of $\Delta\mu_O$. Dashed and dotted lines, respectively, indicate the O-poor and O-rich limits. The top axes show corresponding O_2 pressures at 600 and 800 K.

this point, the system transitions from the perfect surface phase (gray region in Fig. 3**d**) to phase P7 (red region), where an O_2 molecule adsorbs onto a surface Ni site with an adsorption energy of –0.93 eV. A second transition occurs at $\Delta\mu_O \approx -0.21$ eV (corresponding to 3.31×10^2, 4.59×10^4, 9.37×10^6, and 1.79×10^8 atm at 300, 400, 600, and 800 K), which is an unrealistic phase transition from phase P7 into phase P8 (blue region). While the comparison of the formation energy of V_{Ni} suggests that O_2 adsorption promotes V_{Ni} formation by lowering the V_{Ni} formation energy by 0.36 eV, from 3.57 to 3.21 eV. These findings align with experimental observations reporting that excess O_2 environments increase V_{Ni} concentrations, improving electrical and interfacial properties in photovoltaic devices [12].

Fig. 4 presents the surface phase transitions originating from the V_O surface (P1) as the O_2 partial pressure increases. Two major transitions are observed within the examined range of $\Delta\mu_O$. The first transition occurs at $\Delta\mu_O \approx -1.84$ eV, corresponding to O_2 partial pressures of approximately 1.05×10^{-52}, 6.15×10^{-32}, 5.29×10^{-21}, and 6.55×10^{-13} atm at 300, 400, 600, and 800 K, respectively. At this point, the system evolves from phase P1 (Fig. 4**a** and **d**, yellow region) to phase P6 (Fig. 4**b** and **d**, orange region). This transition proceeds via two distinct steps: (i) one oxygen atom from the O_2 molecule fills the original vacancy, and (ii) the second oxygen atom remains adsorbed at a bridging Ni site. Step (i), the vacancy-healing process, is highly exothermic (–4.88 eV), while the adsorbed O atom in step (ii) is relatively unstable, with an associated V_O formation energy of –1.20 eV, suggesting that it may desorb or migrate under thermal excitation. As a result, the net energy change associated with this process is –3.67 eV. This transition indicates that very low concentrations of O_2 partial pressure are enough to heal O-vacancy on the surface. The second transition is observed at $\Delta\mu_O \approx -1.22$ eV, which corresponds to O_2 partial pressures of 6.12×10^{-32}, 2.30×10^{-21}, 1.27×10^{-10}, and 4.01×10^{-5} atm at 300, 400, 600, and 800 K, respectively. Here, phase P6 transitions into phase P8 (Fig. 4**c** and **d**, blue region), the same final phase reached from the perfect NiO(001) surface under O-rich conditions, as shown in Fig. 3**c**. This convergence suggests that further increases in O_2 partial pressure favor the adsorption of an additional O_2 molecule, which promotes V_{Ni} formation and reflects a thermodynamically preferred pathway for Ni-deficiency under oxidizing conditions.

Fig. 5 presents the surface phase transitions originating from the V_{Ni}-NiO(001) surface (P2) as the O_2 partial pressure increases. A single major phase transition is observed near the O-rich limit at $\Delta\mu_O \approx -0.7$ eV, corresponding to O_2 partial pressures of approximately 1.25×10^{-13}, 1.25×10^{-7}, 1.82×10^{-1}, and 2.95×10^2 atm at 300, 400, 600, and 800 K, respectively. At this point, the surface transforms from phase P2 (Fig. 5**a** and **c**, light blue region) to phase P8 (Fig. 5**b** and **c**, dark blue region). In this configuration, an O_2 molecule strongly adsorbs onto a surface Ni site adjacent to the V_{Ni}, with an adsorption energy of –1.40 eV. Compared to the corresponding adsorption on the perfect NiO surface (–1.03 eV), the nearby Ni vacancy enhances the binding strength by 0.37 eV. This result highlights the increased chemical reactivity of V_{Ni} sites toward oxygen species, reinforcing their role in promoting p-type conductivity in nickel oxide.

To investigate how surface defects and oxygen exposure influence the electronic properties of $NiO/NiO_x(001)$, we computed the atom-projected density of states (PDOS) for three representative surface terminations: perfect, V_O, and V_{Ni} surfaces with and without O_2 adsorption, as shown in Fig. 6. For the ideal NiO(001) surface (Fig. 6**a**), the valence band maximum (VBM) is dominated by O 2*p* states, and the conduction band minimum (CBM) by Ni 3*d* states. The Fermi level lies at the top of

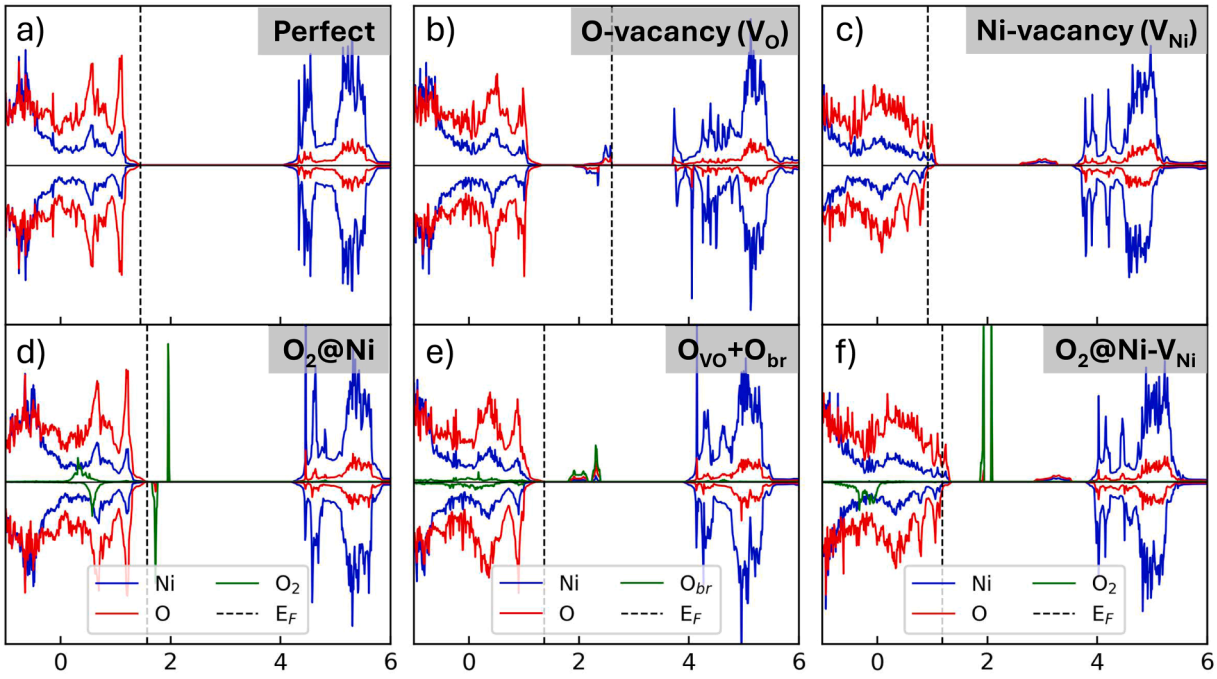

Fig. 6. Atom-projected density of states (PDOS) for six representative NiO/NiO_x(001) surface phases: (a) perfect surface, (b) V_O surface (P1), and (c) V_{Ni} surface (P2); and their corresponding O_2-adsorbed counterparts (d) O_2 on Ni site (P7), (e) bridging O on Ni site (P6), and (f) O_2 on Ni site adjacent to the V_{Ni} (P8). Positive and negative DOS values indicate spin-up and spin-down states, respectively.

the valence band, consistent with the known p-type semiconducting nature of NiO. This band structure agrees with bulk NiO and previous theoretical and experimental findings [36,37]. Upon adsorption of an O_2 molecule (Phase P7, Fig. 6**d**), the O 2*p* states from the O_2 interact with the surface O and Ni states, leading to the formation of localized hybridized states between 1.65 and 2.0 eV. These changes indicate charge transfer from the NiO(001) surface to the O_2 molecule, consistent with the computed relative adsorption energy. Additionally, a sharp unoccupied state just above the Fermi level corresponds to the characteristic orbital of molecular O_2. Despite these interactions, the overall band gap of the system remains largely preserved.

When a V_O is introduced in NiO (phase P1, Fig. 6**b**), it results in a localized defect state near the middle of the band gap. This state is fully occupied, with the Fermi level pinned at its top edge. As such, it represents a deep, neutral defect level rather than a shallow donor. It may act as a trap-assisted recombination center under photoexcitation or charge transfer at the NiO_x/perovskite interface. After O_2 adsorption on the V_O surface (Fig. 6**e**), one oxygen atom fills the vacancy while the other bridges adjacent Ni atoms (phase P6). The 2*p* states of the bridging O strongly hybridize with the valence band, indicating restoration of the lattice oxygen and the formation of deep gap states. These states may function as acceptor-like trap states or serve as active sites for surface chemical reactions.

The V_{Ni} surface (phase P2, Fig. 6**c**) exhibits a significantly modified electronic structure compared to the perfect NiO(001) surface. The removal of surface Ni atoms results in unpaired O 2*p* electrons, leading to a downward shift of the valence band maximum (VBM) and the appearance of shallow, broad-gap states approximately 2.58–3.28 eV below the conduction band minimum (CBM), consistent with previous reports on bulk vacancy defects [36,37]. Additionally, there appear additional tail states near the VBM, acting as acceptor-like levels that facilitate hole doping and thereby enhancing the p-type conductivity of NiO. Following O_2 adsorption near the V_{Ni} site (phase P8), in Fig. 6**f**, sharp and narrow peaks appear at 1.86–2.10 eV above the Fermi level, originating from the orbitals of the molecular O_2. These highly localized states, with little broadening, indicate minimal hybridization with the substrate and suggest that O_2 retains its molecular character. These features resemble those observed in the perfect surface case (Fig. 6d), indicating that the adjacent V_{Ni} does not significantly alter the electronic interaction between O_2 and the surface. The preservation of molecular-like O_2 states and the absence of strong hybridization suggest a physisorbed or weakly chemisorbed configuration. However, the presence of the Ni vacancy still modifies the nearby electronic environment, as evidenced by broader changes in the valence band and enhanced spin asymmetry in the Ni 3*d* and O 2*p* states, which may influence surface reactivity under external stimuli.

Overall, these PDOS results support the thermodynamic and energetic trends observed earlier. Surface-adsorbed O_2 facilitates Ni vacancy formation, leading to electronic structure modifications that strengthen catalytic activity and p-type characteristics. In contrast, O vacancies introduce trap states that reduce hole concentration, but these can be mitigated through O or O_2-driven vacancy healing. Perfect surfaces exhibit only weak interactions with O_2, retaining their electronic structure with minimal perturbation upon adsorption.

4.2. *Surface phase diagram in N_2 environment contribution*

To understand the contribution of N_2 gas to the surface stability of NiO/NiO_x(001), we constructed the surface phase diagram under a background of fixed O_2 partial pressure while systematically varying the N_2 chemical potential. This approach allows us to isolate the specific effect of nitrogen species on surface thermodynamics.

Using the same three basis surface models, we evaluated the adsorption and substitution behavior of nitrogen species on these surfaces. We first considered nitrogen substitution at surface oxygen vacancies (V_O) (Fig. 7**b**), motivated by experimental reports that N-doping improves NiO_x conductivity, particularly when introduced through reactive nitrogen precursors such as guanidine nitrate [38]. However, typical N-incorporation relies on processes generating reactive N species, such as solution processing [38], reactive magnetron sputtering [39], or RF sputtering in Ar–O_2–N_2 plasma [40].

To assess ambient N_2 doping during thermal annealing, which lacks these reactive species, we examined N_2 dissociation pathways on NiO_x(001), given its strong triple bond (gas-phase dissociation energy of

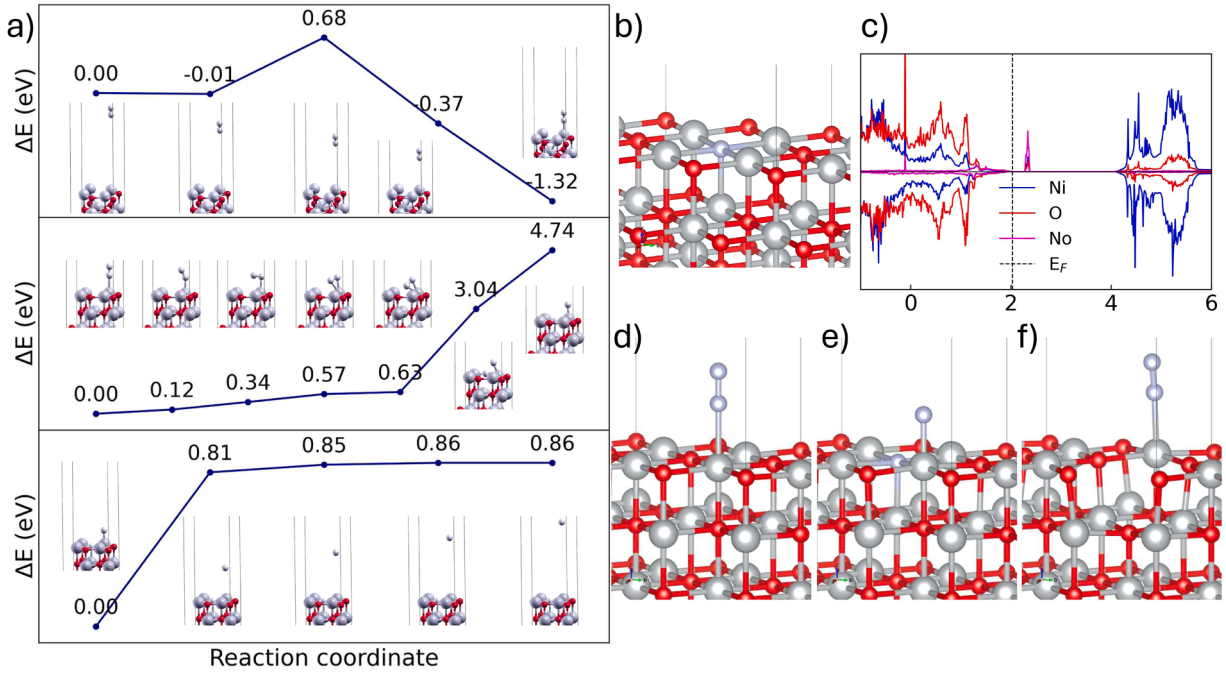

Fig. 7. (a) NEB pathway and energy profile for V_O-assisted N_2 dissociation leading to the N-filled V_O (N_O) configuration, with the relaxed structure shown in (b) and its atom-projected DOS in (c). Gray, red, and blue atoms represent Ni, O, and N, respectively. Panels (d–f) show the relaxed structures of the N_2@Ni, NO–N@Ni, and N_2@Ni–V_{Ni} configurations, respectively.

9.76 eV [41]) compared to O_2 (5.12 eV [42]).

DFT nudged elastic band (NEB) calculations reveal gas-phase dissociation barriers of 6.03 eV for O_2 and 10.77 eV for N_2, matching experimental trends above. On the NiO_x surface, direct N_2 dissociation at Ni sites exceeds 13 eV (**Figure S18**), but V_O-assisted dissociation lowers this to 4.74 eV (Fig. 7**a**). Despite the lower V_O-assisted barrier, the total energy pathways favor O_2 healing V_O (−4.87 eV net kinetic barrier: O_2 adsorption of −3.67 eV + O_{br} removal of −1.20 eV; see Table 3, cases P4 and P6) over N_2 doping (4.28 eV net kinetic barrier: N_2 adsorption of −1.32 eV + dissociation of 4.74 eV + N removal of 0.86 eV; Fig. 7). These results demonstrate that ambient N_2 cannot provide atomic nitrogen, and therefore thermal annealing in N_2 does not result in nitrogen doping. Instead, the role of inert N_2 gas is primarily to influence the O_2 partial pressure and thereby tune the surface oxygen stoichiometry [9].

As shown in the atom-projected DOS (Fig. 7**c**), the N-filled V_O (N_O) configuration exhibits an electronic structure that is clearly different from both the ideal surface and the O-filled vacancy. Specifically, the N_O (magenta line) introduces a localized state around 2.33 eV above the Fermi level, arising from hybridization with neighboring Ni and O atoms. Unlike the perfect surface, where the valence band maximum is primarily composed of O *p* orbitals (Fig. 6**a**), the N_O configuration shifts the valence edge to be dominated by N *p* states.

Nitrogen incorporation as N^{3-} substitutes O^{2-} sites in the NiO lattice, reducing Ni^{2+} and increasing the concentration of Ni^{3+} to maintain charge neutrality [38]. This mechanism enhances p-type hole transport, analogous to the effect of V_{Ni}-induced Ni^{3+} formation. The PDOS (Fig. 7**c**) reveals that N-derived acceptor states lie ~0.5 eV above the VBM, which at first glance appear to be "deep" hole traps. However, transient absorption spectroscopy on NiO nanoparticles identifies intrinsic Ni^{3+} states at similar energies (0.3–0.5 eV above the VBM) as beneficial surface hole reservoirs rather than detrimental traps [43]. Because these states exhibit slow recombination on the nanosecond timescale, holes trapped in them can relax through Ni^{4+} intermediates and subsequently reinject into neighboring Ni^{2+} sites. These surface Ni^{4+} centers therefore act as transient storage sites that facilitate hole hopping between NiO nanoparticles.

To determine the most reasonable and stable adsorption phases for the N_2 molecule, we select three relaxed configurations relevant to our study. First, N_2 adsorbs directly onto a Ni site (N_2@Ni, Fig. 7**d**). Second is when one nitrogen atom adsorbs on a Ni site and the other fills an adjacent V_O (N_O–N@Ni, Fig. 7**d**). Third is N_2 adsorption on a Ni site adjacent to a V_{Ni} (N_2@Ni-V_{Ni}, Fig. 7**e**). The adsorption energies of these cases are shown in Table 4.

A comparison of N_2 and O_2 adsorption on NiO/NiO_x surfaces reveals that O_2 generally exhibits stronger chemisorption, particularly near V_{Ni} sites, as reflected by its substantially lower adsorption energies. In contrast, N_2 molecules tend to adsorb directly onto Ni sites rather than bridge them like oxygen atoms, and their adsorption is typically weaker due to nitrogen's greater chemical stability.

Fig. 8 shows PDOS for the NiO/NiO_x(001) surface in the three configurations: N_2@Ni, N_O–N@Ni, and N_2@Ni-V_{Ni}. In Fig. 8**a**, the adsorbed N_2-related states (green line) appear as narrow, sharp peaks located ~4.3 eV above the Fermi level. These unbroadened features indicate that the N_2 molecule retains much of its molecular character, with negligible hybridization with surface Ni *d* or O *p* states. This behavior reflects weak physical adsorption (physisorption), where van der Waals interactions dominate, and charge transfer is minimal. No significant modification of the electronic structure near the Fermi level occurs, confirming the inert nature of N_2 in this configuration.

In the N_2@Ni-V_{Ni} configuration (Fig. 8**c**), a similar trend is observed. The N_2 PDOS shows localized states in the conduction band region,

Table 4
Summary of point defect formation and adsorption energies for N_2 molecule on NiO/NiO_x(001) surfaces.

Category	Phase Description	Energy Type	Energy (eV)
Defect Formation	V_{Ni} adjacent to N_2-adsorbed site	ΔE_f	3.50
N_2 Adsorption	N_O with N-on-Ni site (N_O-N@Ni)	ΔE_{ad}	4.43
	N_2-on-Ni site (N_2@Ni)	ΔE_{ad}	–0.26
	N_2-on-Ni site adjacent to V_{Ni} (N_2@Ni-V_{Ni})	ΔE_{ad}	–0.33

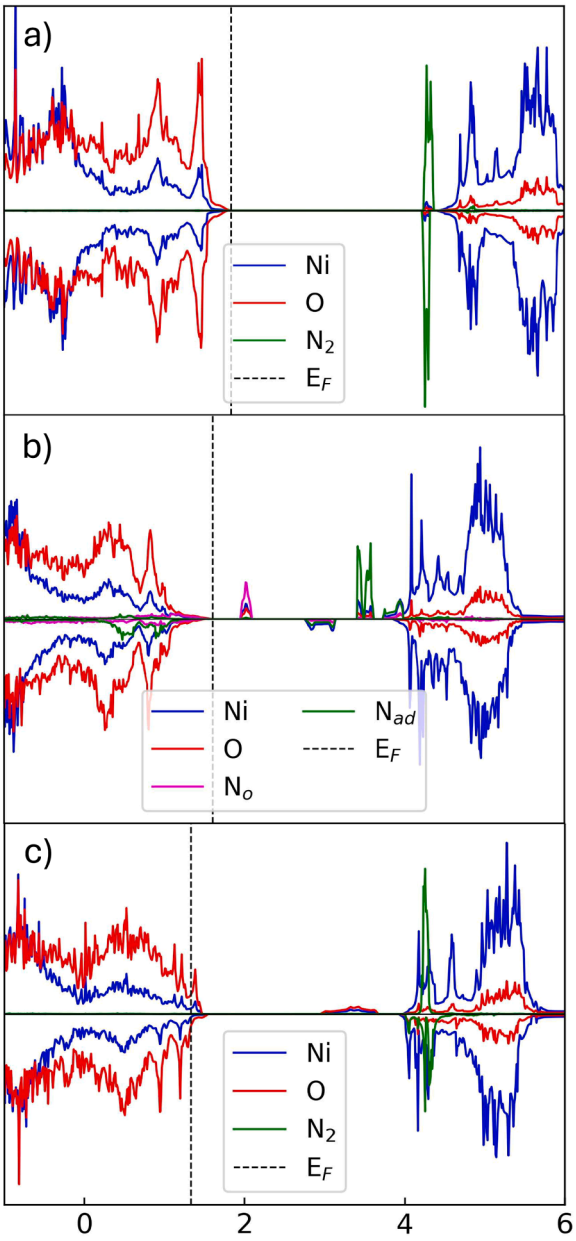

Fig. 8. Atom-projected density of states for the three main studies of NiO/NiO_x(001): (a) N_2@Ni, (b) N_O–N@Ni, and (c) N_2@Ni-V_{Ni}. Positive DOS corresponds to spin-up states, while negative DOS represents spin-down states.

distinct from the surface Ni and O states. The presence of a V_{Ni} does not significantly enhance chemical interaction with N_2, although some weak modulation of the nearby Ni *d* states can be seen. This suggests that the presence of a V_{Ni} slightly perturbs the electronic environment but does not lead to substantial chemisorption or electronic reconstruction. In contrast, N_O–N@Ni configuration (Fig. 8**b**) reveals a fundamentally different interaction. In this configuration, the PDOS contributions from the adsorbed N atom and N_O show broader features near the Fermi level and valence band edge, indicating orbital hybridization. As in the isolated N_O case in Fig. 7**c**, the N_O-induced acceptor states reside ~0.3 eV above the valence band maximum. This condition is accompanied by noticeable hybridization between N *p*, Ni *d*, and O *p* orbitals, particularly in the range from 0 to 1.6 eV. The result is a moderate modification of the valence band edge, with new states that could enhance hole conductivity. Importantly, the N_O defect partially compensates for the deep states introduced by the V_O (Fig. 6**b**), mitigating their recombination activity and restoring favorable p-type behavior. However, this configuration is unlikely to form during thermal annealing due to its high formation energy of 4.43 eV.

These findings highlight the critical role of atomic nitrogen rather than molecular N_2 in modifying the electronic structure of NiO_x surfaces. While molecular N_2 adsorption shows minimal interaction, atomic nitrogen can chemically bond at V_O sites, without causing noticeable lattice distortion. However, effective nitrogen incorporation requires methods that generate reactive atomic nitrogen [38–40,44]. This finding provides a valuable strategy for engineering the surface properties of NiO_x in electronic and photovoltaic applications.

We further performed adsorption studies under O-rich and O-poor conditions to study the phase changes under specific oxygen conditions. For the NiO/NiO_x(001) surface in an N_2 environment, $\Delta\mu_N$ can theoretically decrease without bound[9]. However, we defined a practical range constrained by oxygen:3.3 eV < $\Delta\mu_O$ < 0; nitrogen: $\Delta\mu_N$ < 0), we limit $\Delta\mu_N$ to −3.3 eV, aligning with the O-poor limit. Notably, no phase change occurs below $\Delta\mu_O$ = –2.0 eV in an O_2 environment.

In Fig. 9, dots and solid lines represent adsorption phases under O-rich and O-poor conditions, respectively. The brown line corresponds to molecular N_2 adsorption on a perfect NiO(001) surface, which is largely insensitive to the O_2 partial pressure, indicating a weak interaction with minimal competition from oxygen. In contrast, the magenta line (N_O-N@Ni) shows increasing surface free energy under O-rich conditions, suggesting that this configuration becomes less stable as oxygen competes to occupy the same vacancy sites. This reduced stability reflects a reduced tendency for nitrogen incorporation via defect healing in high-oxygen environments. The green line (N_2@Ni-V_{Ni}) exhibits the opposite behavior: N_2 adsorption becomes more favorable with increasing oxygen potential, as indicated by decreasing surface free energy. This phenomenon could be due to an indirect stabilization effect where O-rich conditions enhance local V_{Ni} structures that favor N_2 adsorption. Finally, the violet line (N_O) becomes significantly less favorable under O-rich conditions due to strong competition from oxygen, which prefers to occupy its native lattice sites and suppress nitrogen incorporation.

We summarize the key findings from Fig. 9 as follows: under O-poor conditions, the most stable phase at high N_2 concentration is the N_2-on-Ni configuration, whereas under O-rich conditions, molecular N_2 adsorption on both perfect and Ni-deficient surfaces (brown and green lines) remains energetically comparable, indicating that these physisorbed states dominate when oxygen competes for vacancy sites.

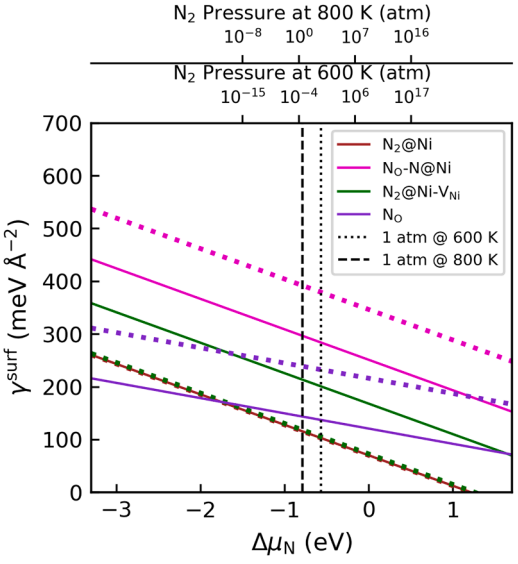

Fig. 9. Surface phase diagram of N_2 adsorption on the NiO/NiO_x(001) surface under O-rich and O-poor conditions. Dots and solid lines represent NiO/NiO_x phases at the O-rich and O-poor limits, respectively.

These results emphasize the interplay between O_2 and N_2 partial pressures in stabilizing or suppressing different nitrogen adsorption configurations. For effective nitrogen doping or defect passivation in NiO_x, maintaining an O-poor atmosphere is crucial, particularly when aiming to introduce nitrogen into oxygen vacancies or form chemically bonded N-O complexes.

4.3. Surface phase diagram in ($\Delta\mu_O$,$\Delta\mu_N$) space

In this section, we extend our investigation into a coupled O_2 and N_2 environment by constructing a comprehensive surface phase diagram of the $NiO/NiO_x(001)$ surface. Unlike in previous sections, where only a single gas environment was considered or one species was treated as a fixed reference, this section's analysis captures the full thermodynamic interplay between $\Delta\mu_O$ and $\Delta\mu_N$. Fig. 10 presents the surface free energies of ten representative surface configurations in the $\Delta\mu_O$ and $\Delta\mu_N$ space. This three-dimensional phase diagram offers a more complete understanding of the phase stability and transformation pathways of $NiO/NiO_x(001)$ surfaces under varying O_2 and N_2 conditions, providing a useful guide for surface engineering strategies such as post-deposition annealing or doping.

Based on the surface free energies in Fig. 10, the resulting surface phase diagram is plotted in Fig. 11, where the lower limits of $\Delta\mu_O$ and $\Delta\mu_N$ have been adjusted to –0.7 eV and –0.3 eV, respectively. This two-dimensional surface phase diagram is constructed by selecting only the lowest energy phase for each ($\Delta\mu_O$, $\Delta\mu_N$) grid point. To simplify the analysis, we exclude minor phases that appear at phase boundaries due to their transient and unstable nature. Four dominant surface phases are identified and analyzed in terms of their dependence on oxygen and nitrogen chemical potentials: N_2@Ni-V_{Ni} (green), N_2@Ni (brown), V_{Ni} (light blue), and O_2@Ni-V_{Ni} (blue). The distinct regions indicate the thermodynamically favored phases, with corresponding O_2 and N_2 partial pressure scales at 300 and 600 K (calculated via Eqs. (7) and (8)) to facilitate translation to experimental conditions. The analysis covers the typical annealing range of 300–800 K, with additional data provided in **Figures S12–S17** of the Supporting Information.

Fig. 11 summarizes the surface stability regions as functions of $\Delta\mu_O$ and $\Delta\mu_N$. Under O-poor conditions ($\Delta\mu_O < -0.47$ eV), the N_2@Ni–V_{Ni} configuration is the most stable, reflecting the strong preference of N_2 to bind at Ni-vacancy sites when oxygen is scarce. As $\Delta\mu_N$ increases, the surface shifts briefly to the N_2@Ni phase, although this region is thermodynamically narrow. In the intermediate region (-0.47 eV $< \Delta\mu_O < -0.20$ eV), the bare V_{Ni} surface is thermodynamically favored. At higher oxygen chemical potential difference ($\Delta\mu_O > -0.20$ eV), the O_2@Ni–V_{Ni} phase becomes dominant, with O_2 strongly stabilizing Ni vacancies.

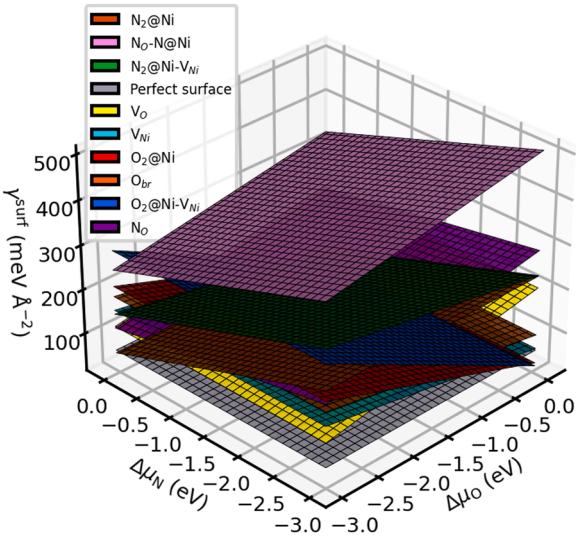

Fig. 10. Surface free energies of the ten stable geometries as a function of $\Delta\mu_O$ and $\Delta\mu_N$. Colors indicate the corresponding surface phases: brown (N_2@Ni), magenta (N_O-N@Ni), green (N_2@Ni-V_{Ni}), grey (perfect surface), yellow (V_O), light blue (V_{Ni}), red (O_2@Ni), orange (O_{br}), blue (O_2@Ni-V_{Ni}), and violet (N_O).

Temperature affects the mapping between chemical potentials and gas partial pressures. At higher temperatures, the same $\Delta\mu_O$ corresponds to higher P_{O_2}, shifting the experimentally accessible 1-atm line toward more O-poor regions. Under realistic annealing conditions (10^{-6}–1 atm of P_{O_2}), the stable high-temperature phase is typically N_2@Ni–V_{Ni}. Upon cooling to room temperature, the system enters the stability region of the V_{Ni} surface, consistent with reports that high-temperature annealing promotes Ni-vacancy formation [12]. Under O-rich annealing, the surface converges to the O_2@Ni–V_{Ni} state, which remains stable upon cooling due to its broad thermodynamic stability region.

We note that several phase boundaries occur at oxygen partial pressures as low as 10^{-23} atm. While these regions follow from the thermodynamic formalism, they are not experimentally accessible and should be interpreted only as limiting cases. The phases most relevant to experiments are those stable between 10^{-6} and 1 atm, where our model predicts transitions between N_2@Ni–V_{Ni}, V_{Ni}, and O_2@Ni–V_{Ni} depending on oxygen stoichiometry.

These findings provide important guidance for the controlled engineering of NiO_x surfaces, especially in applications involving post-deposition annealing, doping, or catalytic activation. The predominance of V_{Ni}-related phases across wide ranges of $\Delta\mu_O$ and $\Delta\mu_N$ suggests that defect-assisted adsorption processes are central to surface reactivity. In particular, the enhanced stability of N_2 and O_2 molecules near Ni vacancies emphasizes the functional role of intrinsic defects in modulating chemical interactions on the surface. Moreover, the ability to selectively stabilize different surface phases by adjusting the O_2/N_2 ratio and temperature presents a powerful strategy for engineering surface electronic properties. For example, the V_{Ni} phase is beneficial for p-type conductivity, while molecular nitrogen incorporation near vacancies may tune surface dipoles or introduce shallow acceptor states, relevant for photovoltaic or sensing applications.

4.4. Discussion and outlook

NiO_x is a complex material system that may contain multiple nickel oxide phases (NiO, NiO_2, NiOOH) [45]. Here we focus on pure NiO to establish a clear atomic-scale understanding of surface defects under O_2/N_2 environments. Experimentally, NiO_x films exhibit a VBM of ~5.2–5.3 eV [9,46], close to $MAPbI_3$ (~5.2 eV) [47]. Early NiO_x/-$MAPbI_3$ devices therefore attempted to raise the NiO_x VBM (via O-poor annealing) to minimize the hole-injection barrier [9]. Our results, however, show that if V_O are not healed by ambient oxygen, they reduce p-type conductivity and introduce mid-gap trap states—explaining the poorer fill factor and stability commonly observed in early $MAPbI_3$ devices.

In modern, high-efficiency triple-cation perovskites, the perovskite VBM is substantially deeper (5.3–5.7 eV) [48]. For such absorbers, NiO_x must instead have a deeper VBM to achieve favorable band offset and suppress interfacial charge accumulation. To examine relative VBM shifts among our NiO surface phases, we aligned the PDOS using the deep O 2*s* state as a reference. A summary of the VBM shifts for all configurations is presented in Fig. 12. We find that V_{Ni}-containing surfaces—regardless of N_2 or O_2 adsorption—exhibit a downward VBM shift of -0.04 to -1.4 eV. These trends are in excellent agreement with experiments reporting VBM lowering under O-rich conditions (e.g., Haider et al. showed a 0.1 eV downward shift [9]) and PLD studies where higher O_2 partial pressure deepens the NiO_x VBM [11].

Although substitutional nitrogen produces acceptor and tail states consistent with Ni^{3+}-related surface states observed by D'Amario et al. [43], it unexpectedly raises the VBM by ~0.4 eV in our calculations—opposite to the downward trend reported by P. Zhou et al. [38].

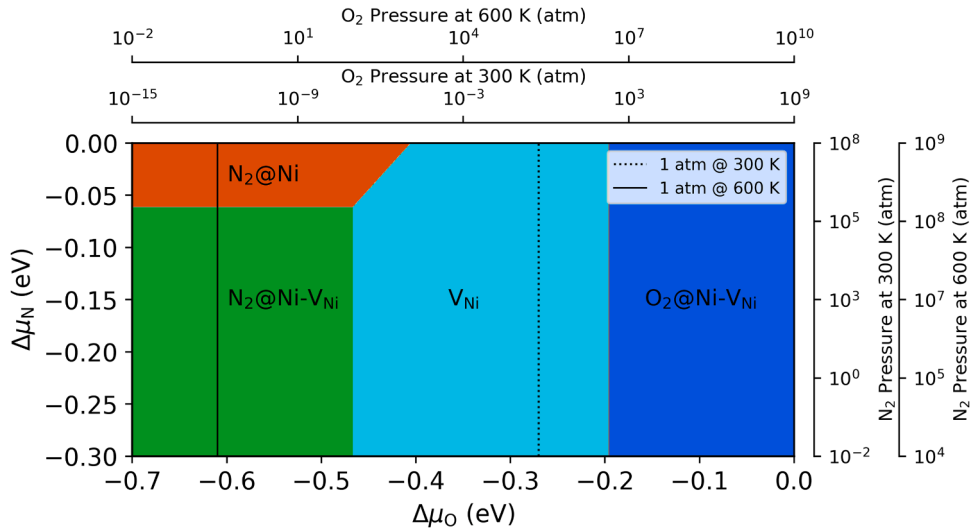

Fig. 11. Surface phase diagram of $NiO/NiO_x(001)$ in ($\Delta\mu_O$, $\Delta\mu_N$) space, highlighting four dominant surface phases across the range from O/N-poor to O/N-rich limits. Additional axes provide corresponding pressure scales at 300 and 600 K. Small-phase coexistence near phase boundaries is considered negligible.

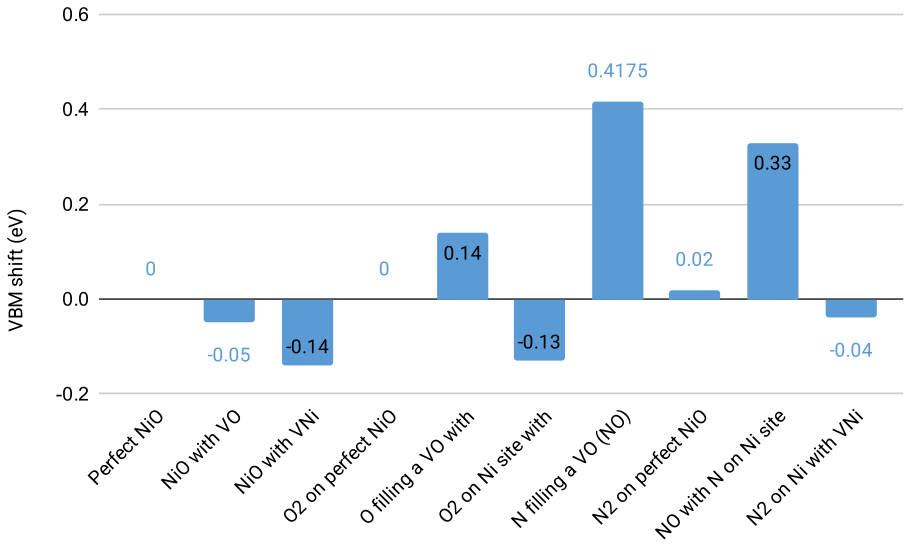

Fig. 12. Valence band maximum (VBM) shift for various NiO surface configurations, including pristine surfaces, oxygen vacancies (V_O), nickel vacancies (V_{Ni}), and adsorbate-modified structures (O_2, N_O, and N_2). Positive values indicate upward band-edge shifts, while negative values correspond to downward shifts.

Combined with our NEB results showing that N_2 cannot dissociate to form N_O during annealing, this suggests that reported "N-doping effects" likely stem from other NiO_x phases (NiO_2/Ni_2O_3) or from processing additives such as guanidinium, consistent with recent findings [49].

While O-rich annealing deepens the VBM and increases hole concentration through V_{Ni} formation, excessive Ni^{3+}/Ni^{4+} species can become chemically reactive toward perovskites, accelerating degradation [45]. Therefore, the optimal O_2/N_2 ratio must balance vacancy healing, p-type enhancement, and interfacial chemical stability. For $MAPbI_3$, for instance, a ratio of $O_2/(O_2+N_2) \approx 30\%$ has been reported to yield the best fill factor and device efficiency [12].

In summary, controlled oxygen stoichiometry is key not only for tuning band alignment and hole extraction but also for preparing a buried NiO_x/perovskite interface that promotes large perovskite grains, reduced trap density, and improved device stability. These insights connect atomic-scale defect energetics directly to experimental trends in power conversion efficiency, fill factor, and long-term stability.

5. Conclusions

In this study, we employed density functional theory combined with *ab initio* atomistic thermodynamics to investigate the thermodynamic stability of NiO_x (001) surfaces in O_2 and N_2 gas environments, conditions relevant for post-deposition annealing in perovskite solar cells. A key methodological advancement introduced here is the SFAE method, which enables efficient and accurate surface free energy calculations for asymmetric slab models, providing a robust alternative to the conventional symmetric slab approach.

Our comprehensive surface phase diagrams reveal that oxygen-rich environments promote the formation of Ni vacancies and facilitate the healing of oxygen vacancies via O_2 adsorption, enhancing p-type conductivity in NiO_x. While substitutional N at oxygen vacancy sites is predicted to introduce acceptor-like states that could enhance hole transport, our results demonstrate that thermal annealing in N_2 cannot provide the reactive atomic nitrogen needed to form these defects. Consequently, effective N incorporation must rely on processes that supply activated nitrogen species, such as solution additives or plasma-

or sputter-based methods. Importantly, molecular N_2 adsorption was found to be weak and reversible, suggesting that only atomic nitrogen species — not molecular N_2—can meaningfully modify the electronic structure of NiO_x surfaces.

By systematically exploring the thermodynamic landscape as a function of O_2 and N_2 chemical potentials, we identify optimal gas-phase conditions and temperatures to stabilize desirable surface terminations. These insights provide valuable guidelines for tailoring NiO_x surface chemistry during annealing, with direct implications for improving the performance and stability of NiO_x-based hole transport layers in inverted perovskite solar cells. Furthermore, the methodology developed in this work offers a general framework for surface phase prediction in multicomponent gas environments and can be extended to other catalytic or electronic oxide materials.

Funding sources

This research project was supported by King Mongkut's University of Technology Thonburi (KMUTT), Thailand Science Research and Innovation (TSRI), and the National Science, Research, and Innovation Fund (NSRF) Fiscal Year 2025 (Grant number FRB680074/0164). W.R. acknowledges support from the Petchra Pra Jom Klao Master's Degree Scholarship, KMUTT.

Declaration of generative AI and AI-assisted technologies in the manuscript preparation process

During the preparation of this work the author(s) used ChatGPT and QuillBot in order to improve clarity, grammar, and style of the manuscript text. After using this tool/service, the author(s) reviewed and edited the content as needed and take(s) full responsibility for the content of the published article.

CRediT authorship contribution statement

Waranchit Ruengsrisang: Writing – original draft, Visualization, Methodology, Formal analysis, Data curation, Conceptualization. **Pakpoom Reunchan:** Writing – review & editing, Validation, Supervision. **Watchara Liewrian:** Writing – review & editing, Validation, Supervision. **Non Thongprong:** Writing – review & editing, Supervision, Resources, Project administration, Funding acquisition.

Declaration of competing interest

The authors declare the following financial interests/personal relationships which may be considered as potential competing interests:

Non Thongprong reports financial support was provided by Thailand Science Research and Innovation. If there are other authors, they declare that they have no known competing financial interests or personal relationships that could have appeared to influence the work reported in this paper.

Acknowledgment

This research project was supported by King Mongkut's University of Technology Thonburi (KMUTT), Thailand Science Research and Innovation (TSRI), and the National Science, Research, and Innovation Fund (NSRF) Fiscal Year 2025 (Grant number FRB680074/0164). W.R. acknowledges the Petchra Pra Jom Klao Master's Degree Scholarship from King Mongkut's University of Technology Thonburi (KMUTT).

Supplementary materials

Supplementary material associated with this article can be found, in the online version, at doi:10.1016/j.surfin.2026.109055.

Data availability

Data will be made available on request.

References

[1] J.-H. Im, I.-H. Jang, N. Pellet, M. Grätzel, N.-G. Park, Growth of CH3NH3PbI3 cuboids with controlled size for high-efficiency perovskite solar cells, Nat. Nanotechnol. 9 (2014) 927–932, https://doi.org/10.1038/nnano.2014.181.
[2] M. Liu, M.B. Johnston, H.J. Snaith, Efficient planar heterojunction perovskite solar cells by vapour deposition, Nature 501 (2013) 395–398, https://doi.org/10.1038/nature12509.
[3] J. Burschka, N. Pellet, S.-J. Moon, R. Humphry-Baker, P. Gao, M.K. Nazeeruddin, M. Grätzel, Sequential deposition as a route to high-performance perovskite-sensitized solar cells, Nature 499 (2013) 316–319, https://doi.org/10.1038/nature12340.
[4] X. Yin, Z. Yao, Q. Luo, X. Dai, Y. Zhou, Y. Zhang, Y. Zhou, S. Luo, J. Li, N. Wang, High efficiency inverted planar perovskite solar cells with solution-processed NiO x hole contact, ACS Appl. Mater. Interfaces 9 (2017) 2439–2448, https://doi.org/10.1021/acsami.6b13372.
[5] Y. Zhao, K. Zhu, Organic–inorganic hybrid lead halide perovskites for optoelectronic and electronic applications, Chem. Soc. Rev. 45 (2016) 655–689, https://doi.org/10.1039/C4CS00458B.
[6] Y. Liu, B. Ding, G. Zhang, X. Ma, Y. Wang, X. Zhang, L. Zeng, M.K. Nazeeruddin, G. Yang, B. Chen, Synergistic redox modulation for high-performance nickel oxide-based inverted perovskite solar modules, Adv. Sci. 11 (2024) 2309111, https://doi.org/10.1002/advs.202309111.
[7] P.P. Rajbhandari, B. Rijal, Z. Chen, A. Choudhary, H. Efstathiadis, T.P. Dhakal, Performance enhancement of inverted perovskite solar cells through lithium-ion diffusion from the nickel oxide hole transport layer to the perovskite absorber, Energy Adv. (2025), https://doi.org/10.1039/D5YA00072F.
[8] Y. Yoo, H. Jung, H.J. Park, J. Kim, K.S. Jung, H.R. Lee, J. Byeon, H. Lee, W. Cho, S. H. Kim, Oxidation state manipulation of NiOx for high performance and light-soaking stability of perovskite solar modules, Small Methods (2025) e01325, https://doi.org/10.1002/smtd.202501325.
[9] M.I. Haider, A. Fakharuddin, S. Ahmed, M. Sultan, L. Schmidt-Mende, Modulating defect density of NiO hole transport layer via tuning interfacial oxygen stoichiometry in perovskite solar cells, Sol. Energy 233 (2022) 326–336, https://doi.org/10.1016/j.solener.2022.01.023.
[10] H.-J. Seok, J.-H. Park, A. Yi, H. Lee, J. Kang, H.J. Kim, H.-K. Kim, Transition of the NiO x buffer layer from a p-type semiconductor to an insulator for operation of perovskite solar cells, ACS Appl. Energy Mater. 4 (2021) 5452–5465, https://doi.org/10.1021/acsaem.1c00049.
[11] M. Feng, M. Wang, H. Zhou, W. Li, X. Xie, S. Wang, Z. Zang, S. Chen, Optoelectronic modulation of undoped NiO x films for inverted perovskite solar cells via intrinsic defect regulation, ACS Appl. Energy Mater. 3 (2020) 9732–9741, https://doi.org/10.1021/acsaem.0c01330.
[12] X. Zhao, J. Chen, N.G. Park, Importance of oxygen partial pressure in annealing NiO film for high efficiency inverted perovskite solar cells, Sol. RRL 3 (2019) 1800339, https://doi.org/10.1002/solr.201800339.
[13] K. Reuter, M. Scheffler, Composition, structure, and stability of RuO 2 (110) as a function of oxygen pressure, Phys. Rev. B 65 (2001) 035406, https://doi.org/10.1103/PhysRevB.65.035406.
[14] K. Reuter, M. Scheffler, Composition and structure of the RuO 2 (110) surface in an O 2 and CO environment: implications for the catalytic formation of CO 2, Phys. Rev. B 68 (2003) 045407, https://doi.org/10.1103/PhysRevB.68.045407.
[15] N.M. Stuart, K. Sohlberg, A method of calculating surface energies for asymmetric slab models, Phys. Chem. Chem. Phys. 25 (2023) 13351–13358, https://doi.org/10.1039/D2CP04460A.
[16] G. Sawatzky, J. Allen, Magnitude and origin of the band gap in NiO, Phys. Rev. Lett. 53 (1984) 2339, https://doi.org/10.1103/PhysRevLett.53.2339.
[17] A. Cheetham, D. Hope, Magnetic ordering and exchange effects in the antiferromagnetic solid solutions Mn x Ni 1− x O, Phys. Rev. B 27 (1983) 6964, https://doi.org/10.1103/PhysRevB.27.6964.
[18] B. Fender, A. Jacobson, F. Wedgwood, Covalency parameters in MnO, α-MnS, and NiO, J. Chem. Phys. 48 (1968) 990–994, https://doi.org/10.1063/1.1668855.
[19] P. Giannozzi, S. Baroni, N. Bonini, M. Calandra, R. Car, C. Cavazzoni, D. Ceresoli, G.L. Chiarotti, M. Cococcioni, I. Dabo, QUANTUM ESPRESSO: a modular and open-source software project for quantumsimulations of materials, J. Phys.: Condens. Matter 21 (2009) 395502, https://doi.org/10.1088/0953-8984/21/39/395502.
[20] J.P. Perdew, K. Burke, M. Ernzerhof, Generalized gradient approximation made simple, Phys. Rev. Lett. 77 (1996) 3865, https://doi.org/10.1103/PhysRevLett.77.3865.
[21] J.P. Perdew, A. Ruzsinszky, G.I. Csonka, O.A. Vydrov, G.E. Scuseria, L. A. Constantin, X. Zhou, K. Burke, Restoring the density-gradient expansion for exchange in solids and surfaces, Phys. Rev. Lett. 100 (2008) 136406, https://doi.org/10.1103/PhysRevLett.100.136406.
[22] P.E. Blöchl, O. Jepsen, O.K. Andersen, Improved tetrahedron method for Brillouin-zone integrations, Phys. Rev. B 49 (1994) 16223, https://doi.org/10.1103/PhysRevB.49.16223.
[23] H.J. Monkhorst, J.D. Pack, Special points for Brillouin-zone integrations, Phys. Rev. B 13 (1976) 5188, https://doi.org/10.1103/PhysRevB.13.5188.
[24] B. Walls, A. Mazilkin, B. Mukhamedov, A. Ionov, I. Smirnova, A. Ponomareva, K. Fleischer, N. Kozlovskaya, D. Shulyatev, I. Abrikosov, Nanodomain structure of

single crystalline nickel oxide, Sci. Rep. 11 (2021) 3496, https://doi.org/10.1038/s41598-021-82070-1.
[25] D. Ködderitzsch, W. Hergert, W. Temmerman, Z. Szotek, A. Ernst, H. Winter, Exchange interactions in NiO and at the NiO (100) surface, Phys. Rev. B 66 (2002) 064434, https://doi.org/10.1103/PhysRevB.66.064434.
[26] B. Wang, J. Nisar, R. Ahuja, Molecular simulation for gas adsorption at NiO (100) surface, ACS Appl. Mater. Interfaces 4 (2012) 5691–5697, https://doi.org/10.1021/am3016894.
[27] S. Jiang, S.H. Mushrif, Determining surface-specific Hubbard-U corrections and identifying key adsorbates on nickel and cobalt oxide catalyst surfaces, Phys. Chem. Chem. Phys. 25 (2023) 8903–8912, https://doi.org/10.1039/D2CP04814K.
[28] S. Grimme, J. Antony, S. Ehrlich, H. Krieg, A consistent and accurate ab initio parametrization of density functional dispersion correction (DFT-D) for the 94 elements H-Pu, J. Chem. Phys. 132 (2010), https://doi.org/10.1063/1.3382344.
[29] S.-N. Hong, Y.-H. Kye, C.-J. Yu, U.-G. Jong, G.-C. Ri, C.-S. Choe, K.-H. Kim, J.-M. Han, Ab initio thermodynamic study of the SnO 2 (110) surface in an O 2 and NO environment: a fundamental understanding of the gas sensing mechanism for NO and NO 2, Phys. Chem. Chem. Phys. 18 (2016) 31566–31578, https://doi.org/10.1039/C6CP05433A.
[30] W.M. Haynes, CRC Handbook of Chemistry and Physics, CRC press, 2016, https://doi.org/10.1201/9781315380476.
[31] A. Schrön, M. Granovskij, F. Bechstedt, Influence of on-site Coulomb interaction U on properties of MnO (001) 2× 1 and NiO (001) 2× 1 surfaces, J. Phys.: Condens. Matter 25 (2013) 094006, https://doi.org/10.1088/0953-8984/25/9/094006.
[32] I. Leonov, S. Biermann, Electronic correlations at paramagnetic (001) and (110) NiO surfaces: charge-transfer and Mott-Hubbard-type gaps at the surface and subsurface of (110) NiO, Phys. Rev. B 103 (2021) 165108, https://doi.org/10.1103/PhysRevB.103.165108.
[33] A. Schrön, F. Bechstedt, Spin-dependent properties and images of MnO, FeO, CoO, and NiO (001) surfaces, Phys. Rev. B 92 (2015) 165112, https://doi.org/10.1103/PhysRevB.92.165112.
[34] O. Bengone, M. Alouani, J. Hugel, P. Blöchl, LDA+ U calculated electronic and structural properties of NiO (0 0 1) and NiO (1 1 1) p (2× 2) surfaces, Comput. Mater. Sci. 24 (2002) 192–198, https://doi.org/10.1016/S0927-0256(02)00186-6.
[35] W.-B. Zhang, N. Yu, W.-Y. Yu, B.-Y. Tang, Stability and magnetism of vacancy in NiO: a GGA+ U study, Eur. Phys. J. B 64 (2008) 153–158, https://doi.org/10.1140/epjb/e2008-00303-x.
[36] E. Aydin, J. Troughton, M. De Bastiani, E. Ugur, M. Sajjad, A. Alzahrani, M. Neophytou, U. Schwingenschlogl, F. Laquai, D. Baran, Room-temperature-sputtered nanocrystalline nickel oxide as hole transport layer for p–i–n perovskite solar cells, ACS Appl. Energy Mater. 1 (2018) 6227–6233, https://doi.org/10.1021/acsaem.8b01263.
[37] W. Chen, Y. Wu, J. Fan, A.B. Djurišić, F. Liu, H.W. Tam, A. Ng, C. Surya, W.K. Chan, D. Wang, Understanding the doping effect on NiO: toward high-performance inverted perovskite solar cells, Adv. Energy Mater. 8 (2018) 1703519, https://doi.org/10.1002/aenm.201703519.
[38] P. Zhou, B. Li, Z. Fang, W. Zhou, M. Zhang, W. Hu, T. Chen, Z. Xiao, S. Yang, Nitrogen-doped nickel oxide as hole transport layer for high-efficiency inverted planar perovskite solar cells, Sol. RRL 3 (2019) 1900164, https://doi.org/10.1002/solr.201900164.
[39] J. Keraudy, A. Ferrec, M. Richard-Plouet, J. Hamon, A. Goullet, P.-Y. Jouan, Nitrogen doping on NiO by reactive magnetron sputtering: a new pathway to dynamically tune the optical and electrical properties, Appl. Surf. Sci. 409 (2017) 77–84, https://doi.org/10.1016/j.apsusc.2017.02.229.
[40] M. Dragoman, S. Vulpe, E. Aperathithis, C. Aivalioti, C. Romanitan, A. Dinescu, D. Dragoman, M. Aldrigo, N. Djourelov, M. Modreanu, Oxygen-vacancy induced ferroelectricity in nitrogen-doped nickel oxide, J. Appl. Phys. 131 (2022), https://doi.org/10.1063/5.0075568.
[41] P. Wang, S. Gong, Y. Li, Y. Mo, Bond dissociation energy of N2 measured by state-to-state resolved threshold fragment yield spectra, J. Chem. Phys. 160 (2024), https://doi.org/10.1063/5.0187003.
[42] P. Wang, S. Gong, Y. Mo, Bond dissociation energy of O2 measured by fully state-to-state resolved threshold fragment yield spectra, J. Chem. Phys. 160 (2024), https://doi.org/10.1063/5.0187003.
[43] L. D'Amario, J. Föhlinger, G. Boschloo, L. Hammarström, Unveiling hole trapping and surface dynamics of NiO nanoparticles, Chem. Sci. 9 (2018) 223–230, https://doi.org/10.1039/C7SC03442C.
[44] Y. Hu, J. Lu, H. Feng, Surface modification and functionalization of powder materials by atomic layer deposition: a review, RSC Adv. 11 (2021) 11918–11942, https://doi.org/10.1039/D1RA00326G.
[45] M. Du, S. Zhao, L. Duan, Y. Cao, H. Wang, Y. Sun, L. Wang, X. Zhu, J. Feng, L. Liu, Surface redox engineering of vacuum-deposited NiOx for top-performance perovskite solar cells and modules, Joule 6 (2022) 1931–1943, https://doi.org/10.1016/j.joule.2022.06.026.
[46] A. Itzhak, X. He, A. Kama, S. Kumar, M. Ejgenberg, A. Kahn, D. Cahen, NiN-passivated NiO hole-transport layer improves halide perovskite-based solar cell, ACS Appl. Mater. Interfaces 14 (2022) 47587–47594, https://doi.org/10.1021/acsami.2c11701.
[47] J. Endres, D.A. Egger, M. Kulbak, R.A. Kerner, L. Zhao, S.H. Silver, G. Hodes, B. P. Rand, D. Cahen, L. Kronik, Valence and conduction band densities of states of metal halide perovskites: a combined experimental–theoretical study, J. Phys. Chem. Lett. 7 (2016) 2722–2729, https://doi.org/10.1021/acs.jpclett.6b00946.
[48] K. Amratisha, W. Tuchinda, P. Ruankham, A. Naikaew, P. Pansa-Ngat, L. Srathongsian, W. Wattanathana, K.K. Shin Thant, R. Supruangnet, H. Nakajima, Graded multilayer triple cation perovskites for high speed and detectivity self-powered photodetector via scalable spray coating process, Sci. Rep. 12 (2022) 11058, https://doi.org/10.1038/s41598-022-14774-x.
[49] K.T. Soe, R. Supruangnet, C. Euaruksakul, T. Wongpinij, A.A. Yaro, N. Thongprong, E. Ketsombun, S. Kinkasorn, W. Ruengsrisang, T. Supasai, N. Rujisamphan, Mitigating surface and grain boundary defects in perovskite solar cells through guanidinium halide passivation, Sol. RRL 9 (2025) 2500319, https://doi.org/10.1002/solr.202500319.